#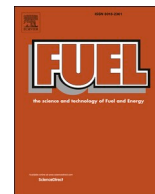 High-Temperature corrosion of P91/T91, 304L, Sanicro 28 and Inconel 625 exposed at 600 °C under continuous KCl deposition

(article starts on next page)

Full Length Article

High-Temperature corrosion of P91/T91, 304L, Sanicro 28 and Inconel 625 exposed at 600 °C under continuous KCl deposition

J. Phother-Simon, I. Hanif, T. Jonsson, J. Liske [*]

Environmental Inorganic Chemistry, Department of Chemistry and Chemical Engineering, Chalmers University of Technology, S-412 96, Göteborg, Sweden

A B S T R A C T

This study investigates the corrosion attack after breakaway oxidation on four commercial alloys (T91/P91, 304L, Sanicro 28 and Inconel 625) in the presence of KCl(g)/KCl(s) at 600 °C. The study suggests that an increase in corrosion resistant alloying elements (mainly nickel and chromium) results in the decrease of the thickness of the general oxide scale and not equally deep alloy grain boundary attack for the austenitic alloys. The corrosion attack in the presence of KCl is suggested to proceed by chromate formation and chlorine-induced acceleration of the diffusion of ions through the scale.

1. Introduction

The increased emission of greenhouse gases in the atmosphere caused by human activities has led to efforts being put forward to reduce this trend. Most of the greenhouse gases originate from the combustion of fossil fuels [1]. One of the main greenhouse gases is carbon dioxide (CO_2) which is greatly contributing to the greenhouse effect. A way to reduce the net emission of CO_2 is the replacement of fossil fuels with renewable fuels in power plants. Unfortunately, the combustion of renewable fuels such as biomass and biogenic waste generally produces corrosive deposits and gases that deteriorate vital parts of the plant. The resulting flue gas consists mainly of water vapor, CO_2, hydrogen chloride and especially alkali chlorides [2–4]. Alkali chlorides are known for their corrosiveness towards superheater tubes [3–21]. The current trend in utilizing more and more agricultural and forestry residues, waste wood, and other waste fractions instead of clean biomass (e.g., wood chips and wood pellets) makes this issue even more pronounced.

The corrosiveness of this type of environment have been proposed to occur by several different mechanisms:

The "active oxidation" mechanism [3,5,22–26] where $Cl_2(g)$ is transported through the oxide scale to the oxide/metal interface. The chlorine then reacts with the metal to form volatile metal chlorides ($MeCl_x(g)$) which diffuse outwards through the oxide scale, via cracks and pores, towards the gas/oxide interface. The mechanism relies on a difference in partial pressure of oxygen over this scale, being higher at the gas/scale interface. When the outwardly diffusing metal chlorides

reaches the gas/scale interface they react with oxygen, releasing chlorine gas and forming iron oxide. The newly released chlorine can then follow the same process in a cyclic manner.

The "chromate formation" mechanism [6,7,9–11,13,15,17,18,20, 21,27] where the alkali initiates the corrosion attack of chromia forming steels, deteriorating the protective chromium-rich layer by the formation of alkali chromate. As the primary protection is lost, the resulting secondary oxide scale formed constitutes the steel's ability to withstand further corrosion.

An electrochemical approach has also been suggested, which consists of a flux of anions, cations and an electronic current instead of a gas transport of $Cl_2(g)$ through the oxide scale [28–30].

The corrosive effect of KCl may also be attributed to the ability of chlorine to promote a less adherent oxide scale, causing cracks to form [19].

Alkali chlorides may also, often in environments with complex deposit and gas compositions, form low-melting point eutectics [27,31].

KCl-rich harsh environments are typically generated during the combustion of certain types of biomass and waste (i.e., municipal waste) and the corrosion attack is often very fast with breakaway corrosion usually starting within hours or days [13]. In this process the primary protection oxide scale, e.g., the thin and slow-growing chromium-rich oxide that forms on stainless steels, is destroyed and the resulting oxide scales will influence further corrosion attack. This type of oxide scale has recently been denoted as a secondary protection oxide scale [19,32]. Thus, optimizing the corrosion resistance properties of the secondary

protection oxide scale is probably of great importance for the lifetime of the material. However, systematic studies targeting the secondary oxide (i.e., the oxide scale after breakaway corrosion) are scarce in the literature.

In this study, four commercial alloys (T91/P91, 304L, Sanicro 28 and Inconel 625) were exposed to a harsh environment with continuous KCl deposition. A setup developed and presented in [21] was used in this study to mimic the continuous deposition of KCl(s) that occurs in biomass- and waste-fired boiler environment, simulating a KCl-rich environment,. The investigated materials were selected in such way that they represent a broad range of material classes: from ferritic/martensitic stainless steel T91/P91 to the austenitic stainless steels 304L and Sanicro 28 to the nickel-based alloy Inconel 625. After exposures, the samples were investigated using a combination of microscopy and diffraction techniques, namely SEM/EDX, BIB, TEM and XRD.

2. Materials and methods

2.1. Sample preparation

The investigated materials were the ferritic/martensitic steel T91/P91, the stainless steels 304L, Sanicro 28 and the nickel-based alloy Inconel 625. The material compositions are given in Table. 1. The selected samples were of 15x15x2 mm with a hole of Ø 1.5 mm drilled at 2 and 7.5 mm from the edges. All samples were grounded with 500 grit SiC papers and then polished with 9, 3, and 1 μm diamond suspension DP-Suspension using DP-Lubricant Yellow from Struers. The samples were finally cleaned with acetone and ethanol in an ultrasonic bathtub Elmasonic P from Elma.

2.2. Exposures

The investigated samples were exposed at 600 °C to 5 % O_2 + 20 % H_2O + N_2 (bal.) under continuous KCl deposition. This was achieved by using a three-zone furnace where an alumina boat filled with KCl(s) was placed upstream at 700 °C (calculated vapor pressure of KCl: 65.9 ppm) and the samples were placed downstream at 600 °C (calculated vapor pressure of KCl: 3.4 ppm). Thus, substantial deposition of KCl on the samples as well as in the samples area occurred during the exposures. The KCl-boat and the samples were placed at the same position and distance for each exposure. The temperatures for these positions were individually controlled before each exposure. The vapor pressure of KCl at the two different temperatures was calculated using FactSage 7.2 and the FTsalt database. The duration of the exposures was 24 h. Each exposure included 3 samples and was repeated at least twice in order to achieve reproducibility. More details about system robustness/reproducibility as well as a corrosion comparison of 304L exposed in this setup compared to exposure with ex-situ added KCl(s) and exposure in a 12 MW waste fired boiler is published in [21].

2.3. Broad ion Beam (BIB)

Leica TIC 3X Broad Ion Beam (BIB) was used to prepare cross-sections with smooth surfaces for post-exposure Scanning Electron Microscopy (SEM) imaging. The BIB uses three argon ion guns for milling. To prepare the sample for the BIB milling, a piece of silicon wafer was mounted on top of the sample surface using Loctite 415 glue. After the glue dried, the sample was cut into two pieces using the Minitom low speed saw from Struers. The BIB machine was operated at 8.0 kV for 8 h.

2.4. Scanning Electron microscopy and Energy Dispersive X-rays (SEM-EDX)

The SEM was performed using a Quanta 200 ESEM FEG from FEI equipped with an Oxford Instruments X-Max^N 80 T Energy Dispersive X-rays (EDX) detector. The 10 kV and 20 kV accelerating voltage used was used for imaging and EDX analysis, respectively. Both types of analyses were performed at a 10 mm working distance.

2.5. Transmission Electron microscopy (TEM)

The TEM was performed using Titan 80–300 from FEI with an accelerating voltage of 300 kV in Scanning TEM (STEM) mode. High-Angle Annular Dark Field (HAADF) imaging was also employed in STEM mode. The micrographs and EDX data were processed using Image J and FEI's Tecnai Imaging and Analysis (TIA) software, respectively.

2.6. X-ray diffraction (XRD)

The X-ray Diffraction (XRD) characterization was performed using a Siemens D5000 with a Göbel mirror. The wavelength used was a specific Cu K$_\alpha$ (λ = 1.54178 Å) and was generated by a copper anode X-ray tube. The incident angle was 7.5° and the measuring range was [10° − 80°].

3. Results

The experimental setup allows a continuous deposition of KCl during exposure and exhibits specific characteristics such as "low" and "high amount of KCl"-areas onto the sample surface, described in [21]. These labels were introduced due to the heterogeneous deposition of KCl onto a sample's surface. "High amount of KCl"-areas are usually associated with more severe corrosion compared to "low amount of KCl"-areas. In this study, only "high amount of KCl"-areas were selected for the investigations.

3.1. Characterization of T91/P91

3.1.1. Plan view analysis

The optical inspection revealed a substantial deposition of KCl(s) particles onto the samples after 24 h of exposure. Plan view SEM imaging showed that the surface was completely covered by KCl crystals for high amount of KCl(s)-areas (~99 % of KCl(s) particles coverage). The topography is non-uniform in these areas: small and large buildups of KCl crystals resulting in a non-planar surface (Fig. 1a), and in a higher magnification image showing buildups of KCl crystals and iron oxide (Fig. 1b, area is marked in Fig. 1a.).

3.1.2. Cross-sectional analysis

A thick outward-growing and inward-growing oxide were observed in Fig. 1c. The outward-growing oxide had a thickness between 15 and 30 μm and exhibits some porosity and small whiskers on the top surface. According to XRD and SEM-EDX point analysis, the outward-growing oxide layer is being characterized as hematite (Fe_2O_3) for the top layer and as magnetite (Fe_3O_4) for the layer beneath hematite. On the

Table 1
Chemical compositions of the four investigated materials in weight percentage (wt. %).

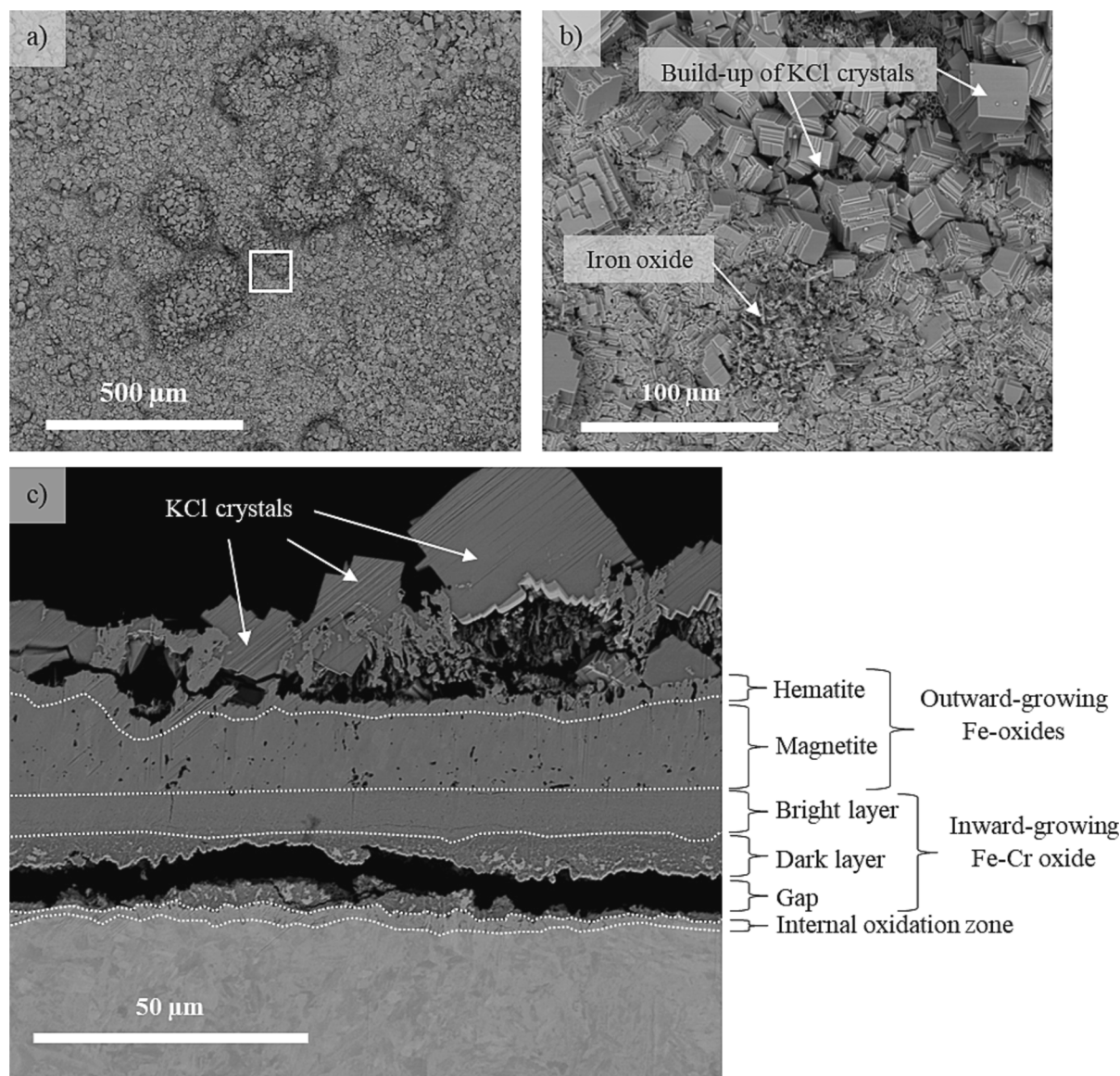| Material	Fe	Cr	Ni	Mn	Si	Mo	N	Cu	P	S	Al	Nb	Ti
T91/P91	Bal.	8.5	0.3	0.6	–	0.85	–	0.1	0.05	0.06	0.15	–	–
304L	Bal.	19.9	10	1.4	0.5	–	–	–	0.05	0.1	–	–	–
Sanicro 28	Bal.	27.5	30.3	1.82	0.5	3.2	0.4	1.2	0.01	0.1	–	–	–
Inconel 625	1.9	23	Bal.	0.1	0.1	9.1	–	–	–	0.07	0.3	3.4	0.3

Fig. 1. a) Plan view SEM image of the surface of T91/P91 after 24 h at 600 °C with continuous KCl(s) deposition. b) Plan view SEM image with high magnification of the marked area in a). c) SEM image of the BIB cross section.

top of the oxide scale, KCl particles can be seen in Fig. 1c. The inward-growing oxide scale consists of several layers, being about 15–25 μm in total. The part located close to the interface of the outward- and inward-growing oxide scale appears brighter (denoted as "bright layer") and more compact than the inward-growing oxide close to the metal/oxide interface (denoted as "dark layer"), see Fig. 1c. A SEM-EDX analysis revealed the brighter and more compact layer in the inward-growing oxide to be a Fe-Cr oxide, dominated by iron (Fe/Cr is about 5, the cationic at. % Cr being 20 %). The darker layer, closer to the substrate material, is composed of Fe-Cr oxide as well with a slightly higher chromium content. The oxide layer is composed of Cr $\sim$ 35 cationic at. % and Fe $\sim$ 65 cationic at. %. The gap within the inward-growing oxide, close to the metal/oxide interface, is suggested to be a result from sample preparation.

A 2.5–3 μm deep internal oxidation zone consisting of dark spots within a brighter matrix was observed at the metal/oxide interface. High magnification image of this zone can be seen in Fig. 2a. This type of corrosion morphology have been reported earlier [15] and is consisting of Fe/Cr rich spinel oxide (dark spots) together with Fe/Ni rich metal (bright matrix). Above the internal oxidation zone, the inward growing

oxide is shown as a dark area. The oxidation front is not completely straight in this higher magnification image, the presence of "metal islands" within the inward-growing oxide can be observed (see Fig. 2a).

A SEM-EDX mapping and point analysis of the internal oxidation zone revealed the presence of chlorine at the metal/oxide interface (see Fig. 2b and c). The presence of chlorine in the SEM-EDX mapping shows a preferential accumulation around the reaction zone "islands" and at the metal/oxide interface. Chlorine was also observed within the inward-growing oxide in relatively low amounts (see Fig. 2c).

3.2. Characterization of 304L

3.2.1. Plan view analysis
The optical inspection revealed the substantial deposition of KCl(s) onto the samples. In the areas of high amount of KCl(s), the plan view SEM imaging revealed a surface mostly covered by KCl crystals when iron oxide is not visible ($\sim$95 % of KCl(s) particles coverage), see Fig. 3a.

3.2.2. Cross-sectional analysis
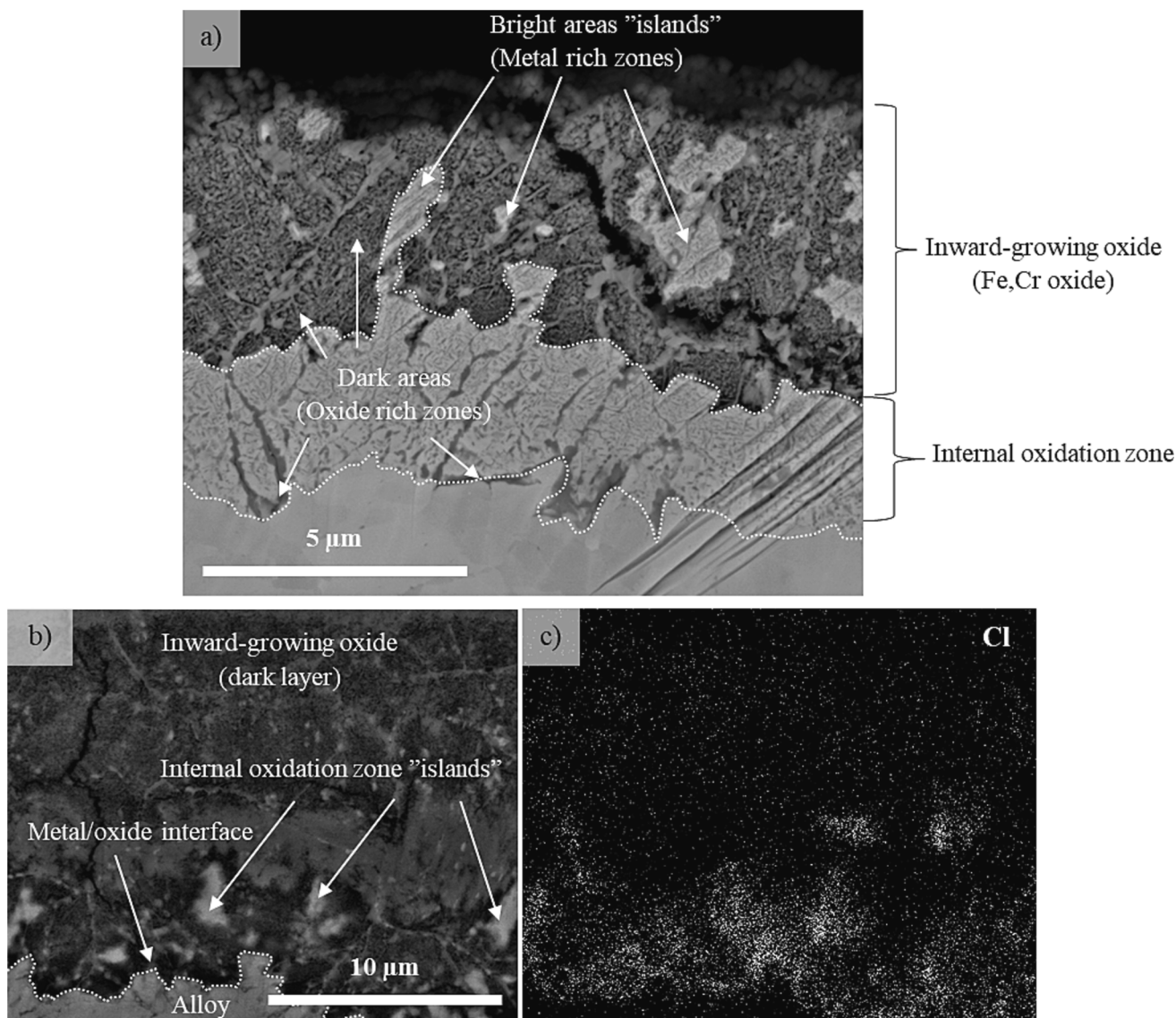The cross-sectional SEM image of 304L showed a less corroded

Fig. 2. a) SEM image of the BIB cross section focusing on the corrosion front of T91/P91 after 24 h at 600 °C with continuous KCl(s) deposition. b) The SEM image coupled to the EDX analysis. c) The EDX map showing Cl.

surface compared to the corresponding T91/P91 sample. From XRD and SEM/EDX analysis, the outward-growing oxide layer (about 3–5 μm thick) was identified as Fe_2O_3 (hematite), see Fig. 3.b and Fig. 3.c. An inward-growing oxide (excluding the steel grain boundary attack) of 2–4 μm thick containing nickel, iron and chromium was also observed. Hence, total thickness of the oxide scales on 304L was about 10 μm, compared to T91/P91 which obtained oxide scales in the range of 40 – 50 μm.

In addition to the oxide scales formed, 304L was also subjected towards steel grain boundary corrosion attack (see Fig. 3.b and Fig. 3.c). In Fig. 3.b the steel grain boundary attack is characterized by a rather narrow and heterogenous oxidation zone along the steel grain boundary. Within this zone, bright nodules rich in nickel were observed together with an oxide consisting primarily of Fe and Cr. In Fig. 3.c the steel grain boundary attack is widened, especially at the top. However, the nickel enriched area is still seen in the middle of the widened area, and it is primarily Fe, Cr oxide that has grown into the steel grain.

The depth of steel grain boundary attacks was ranging from 8 to 50 μm. However, there was no major difference between the deep and shallow steel grain boundary attacks, both exhibited internal oxidation at the grain boundaries with bright nodules in the middle. For 304L, the

corrosion attack in this environment have been thoroughly studied earlier [20,21]. In the articles referred to, the steel GB attack has been investigated with 3D-FIB in combination with SEM/EDX and TEM analysis. Even though the amount of chlorine was small within the GB attack, it was primarily detected at the very tip of the steel GB attack.

3.3. Characterization of Sanicro 28

3.3.1. Plan view analysis

For Sanicro 28, the optical inspection showed less deposition of KCl (s) compared to T91/P91 and 304L (only about 10 % coverage of KCl (s) on Sanicro 28 compared to 95–99 % for 304L and T91/P91). This is confirmed by the plan view SEM observations where a mixture of KCl(s) crystals, iron-rich oxide and potassium chromate was observed on the surface (see Fig. 4a).

3.3.2. Cross-sectional analysis

The SEM analysis of the cross-section of Sanicro 28 is shown in Fig. 4b. As for 304L, the corrosion attack can clearly be distinguished in a general oxidation type corrosion attack and a steel GB corrosion attack. For the general corrosion attack, potassium chromate (K_2CrO_4)
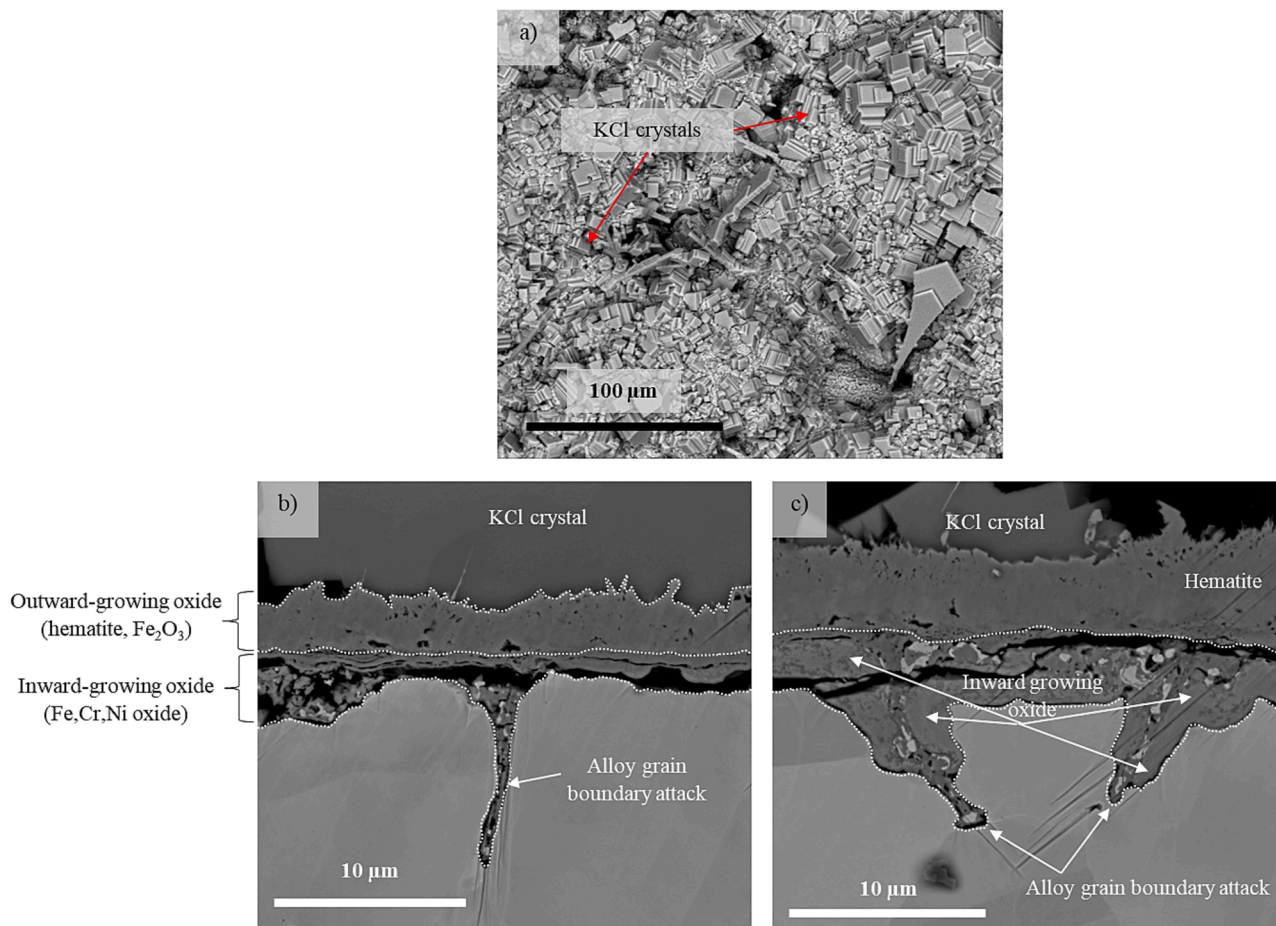
Fig. 3. a) Plan view SEM image of the surface of 304L after 24 h at 600 °C with continuous KCl(s) deposition. b)-c) SEM images of the BIB cross section showing both general corrosion, narrow alloy GB attack (in b) and broad alloy GB attack (in c).
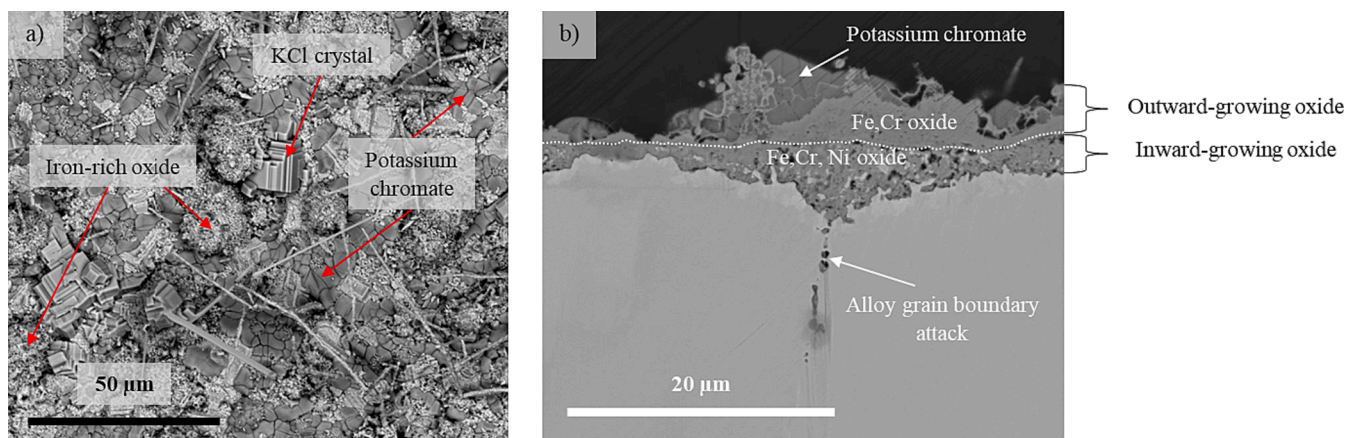

Fig. 4. a) Plan view SEM image of the surface of Sanicro 28 after 24 h at 600 °C with continuous KCl(s) deposition. b) SEM images of the BIB cross section showing both general corrosion and alloy GB attack.

and unreacted potassium chloride (KCl) crystals lay on top of an outward-growing corundum type oxide, according to the combined XRD and SEM analysis. The outward-growing oxide is rich in iron and chromium. Below is an inward-growing oxide which consists of a spinel type oxide rich in chromium, nickel, and iron. The total thickness of the oxide scale is between 3 and 10 μm, which is similar to the thickness of 304L sample.

Besides a general corrosion attack, Sanicro 28 was also subjected towards corrosion attack at the steel grain boundaries (see Fig. 4b). The

typical steel grain boundary attack can be characterized by being wider closer to the surface and becoming narrower (about 0.5–2 μm in width) deeper into the metal substrate. Bright nodules of nickel-rich phases are observable in the steel grain boundary attack. The depth of the grain boundary attacks was between 9 and 18 μm.

An SEM-EDX mapping analysis of the attack is seen in Fig. 5. From the cross-sectional SEM/EDX analysis, an area containing KCl and K_2CrO_4 particles, general corrosion attack and steel grain boundary attacks at two locations can be seen. The analysis shows that Cl can
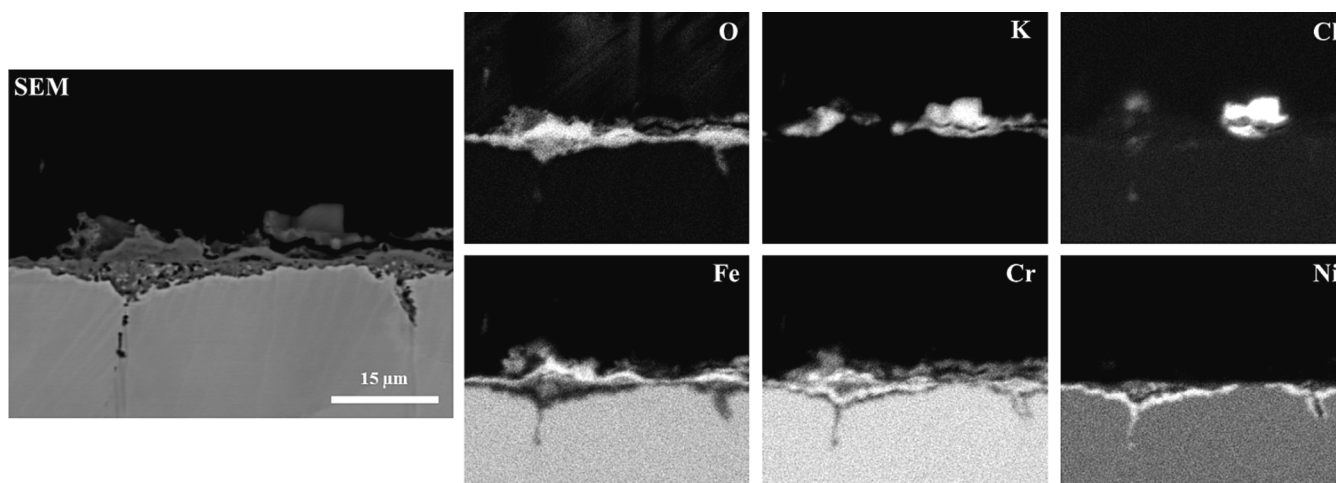
Fig. 5. SEM/EDX analysis of the BIB cross section of Sanicro 28 showing both general corrosion and alloy GB attack.

primarily be detected on the top surface overlapping with K, in the form of KCl. However, trace amounts of Cl, with no K, are also detected in the steel grain boundary attack (to the left). Potassium (K) can be seen not only in the form of KCl but also overlapping with Cr in the form of K_2CrO_4 (particle to the left on the top surface but also in the vicinity of the KCl particle to the right). The outward growing oxide is enriched in Fe and Cr, whereas the inward growing oxide contains besides Fe and Cr also some Ni. In addition, nickel can be seen enriched around the grain boundary attack as well as in the metal close to the metal/oxide interface. SEM-EDX point analyses showed that the composition of the inward-growing oxide and the oxide propagating within the grain boundaries are similar, being most probably a spinel oxide $((Fe,Cr,Ni)_3O_4)$ with the following composition (at.%) O[45–50], Cr[15–20], Fe [15–20] and Ni[20–25].

In contrast to T91/P91 and 304L, the inward-growing oxide formed on Sanicro 28 is less homogeneous, see Fig. 1c., Fig. 3c. and Fig. 4b. Instead of a completely oxidized spinel oxide, the corrosion front of Sanicro 28 is defined by partly oxidized areas mixed with areas being still metallic in character. The metallic parts are enriched in nickel whereas the oxidized areas mainly contain iron and chromium oxide.

3.4. Characterization of Inconel 625

3.4.1. Plan view analysis

The optical inspection of Inconel 625 revealed the similar features observed in the case of Sanicro 28: about ~ 38 % of KCl(s) particles covering the surface. This was also confirmed by the SEM plan view analysis where the surface was only partly covered by KCl(s) (see Fig. 6a). Besides KCl, nickel oxide and potassium chromate were observed on the surface.

3.4.2. Cross-sectional analysis

The BIB cross-section of Inconel 625 is shown in Fig. 6b and Fig. 7. Above the original metal surface, mixed corrosion products consisting of potassium chromate, nickel oxide and chromium-rich oxide was detected. Above these corrosion product layers, deposited KCl was seen. Below the original metal surface, the corrosion attack was defined by internal oxidation zones and alloy grain boundary attacks. The total thickness of the general corrosion scale was about 6 – 12 μm. (see Fig. 6b). In addition to the general corrosion attack, forming outward and inward growing oxide scales, steel grain boundary attack was also observed. Compared to Sanicro 28 and especially 304L, the GB attack was characterized by the formation of voids within the steel grain boundaries to a much higher degree. The size of the voids varied from <
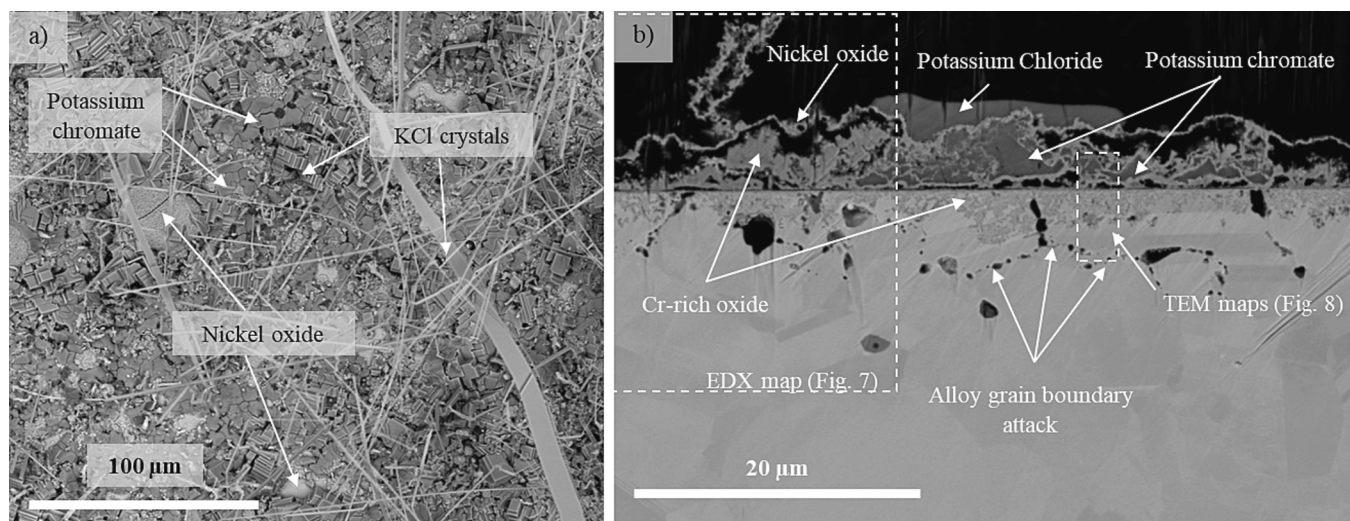

Fig. 6. a) Plan view SEM image of the surface of Inconel 625 after 24 h at 600 °C with continuous KCl(s) deposition. b) SEM images of the BIB cross section showing both general corrosion and alloy GB attack. Areas are marked where SEM/EDX analysis (in Fig. 7) and TEM/EDX analysis (in Fig. 8) have been performed.
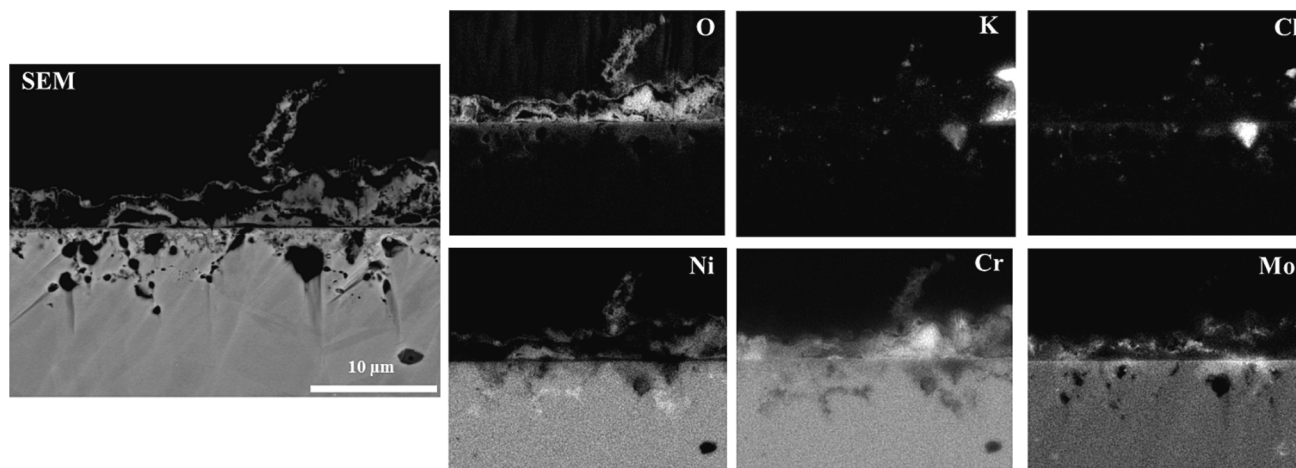
Fig. 7. SEM/EDX analysis of the BIB cross section of Inconel 625 showing both general corrosion and alloy GB attack.

1 μm to 5 μm and reached, as most, a depth of about 11 μm. A SEM-EDX mapping analysis, marked in Fig. 6., is shown in Fig. 7, revealing both the general corrosion attack as well as the GB attack. In addition to the overview shown in Fig. 6b, the analysis indicated that Mo was enriched in the outward growing oxide as well as in the top part of the inward growing oxide scale. The EDX analysis in Fig. 7 also showed some spots in the inward growing scale where Cl was detected without any K. However, the majority of areas with presence of Cl were associated with K and suggested to be in the form of KCl. In order to investigate the corrosion attack on Inconel 625 in more detail higher magnification images using STEM HAADF imaging and EDX were deployed, see Fig. 8 and Fig. 9. The STEM/HAADF/EDX analysis in Fig. 8 confirmed the outward growing oxide to consist of nickel oxide mixed areas of chromium-rich oxide. Above these layers, potassium chromate was detected, see Fig. 8. Within the substrate material, an internal oxidation zone (i.e., not a fully oxidized oxide scale) and a large void was observed. In addition, Cl-enriched spots could be seen throughout the internal oxidation zone as well as below the void. The amount of K in these areas was low. A STEM-EDX linescan over the internal oxidation

zone was performed, see Fig. 9. The analysis revealed a Ni-rich area, about 75 at. % Ni, interrupted by Cr-rich bands. In these bands, the Ni content dropped to about 20–30 at. % whereas the Cr content increased from about 15 at. % to about 45–80 at. %. Throughout the internal oxidation zone, Mo was around 10–15 at. %, except for two bands where the Mo content increased to about 30–50 at. %. According to the line scan, Cl was unevenly distributed and in the range 0–15 at. %.

3.5. Summary of corrosion attack

With respect to key features of the corrosion attack the four materials investigated have been summarized in Table 2.

4. Discussion

The objective of this work is to evaluate and compare the corrosion performance of four commercial alloys in a laboratory environment mimicking key features of the corrosiveness of biomass- and waste-fired boilers. This has been achieved by deploying a continuous KCl
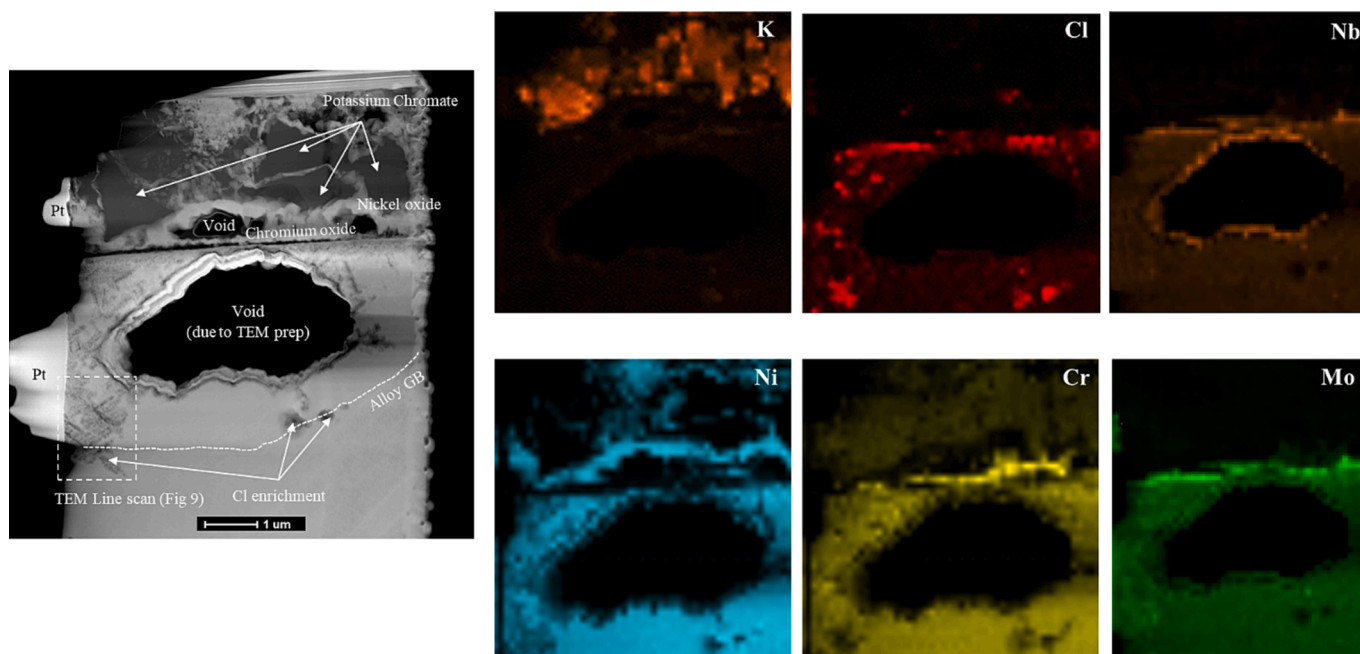

Fig. 8. TEM/EDX analysis of the BIB cross section of Inconel 625 showing both general corrosion and alloy GB attack. An area is marked where TEM Line scan (in Fig. 9) has been performed.
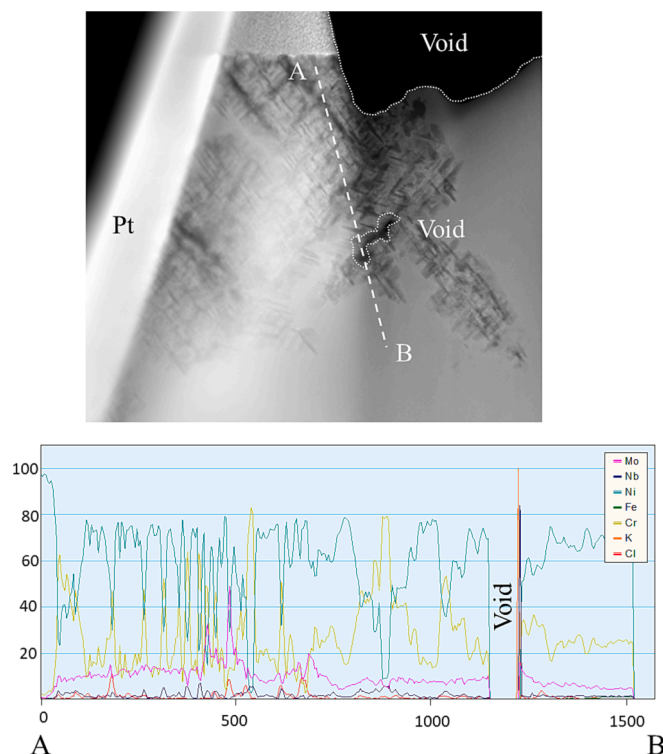
Fig. 9. TEM Line scan analysis of the BIB cross section of Inconel 625 through the internal oxidation zone.

deposition technique presented in [21]. The laboratory setup in [21] was tested for the austenitic stainless steel 304L in order to investigate the initial corrosion attack (24 h) and compare the corrosion attack with corresponding sample exposed to ex-situ added KCl(s) as well as in a 12 MW waste fired boiler. The results in [21] showed that the continuously depositing KCl technique better resemble the corrosion attack of samples exposed in a 12 MW waste fired compared to ex-situ added KCl.
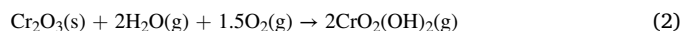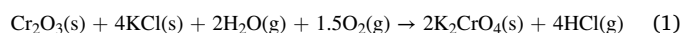
The materials selected for this investigation all possess the ability to form chromia (Cr_2O_3) or Cr-rich corundum type oxide ($(Fe,Cr)_2O_3$) when exposed at high temperatures and mild environments. In addition, the materials were selected to cover a wide spectrum of material classes (ferritic stainless steel, austenitic stainless steels and nickel base alloy). As a general trend for these material classes, the iron content decreases, and the nickel content increases as going from P91/T91 → 304L → Sanicro 28 → Inconel 625. Chromia forming steels/alloys is usually the preferred choice in the most severe corrosive environments in a CHP plant combusting biomass and waste. However, based on short term probe exposures, many of these materials are not sustaining the Cr_2O_3 (or the protective Cr-rich $(Fe,Cr)_2O_3$) for very long [13,33,34]. This time period is referred to as the "primary regime" and for chromia forming steels/alloys the initially formed chromia as the "primary protection" [32]. Instead, these materials suffer from breakaway corrosion and thus, entering into the secondary regime (and the oxide scale is referred to as

the "secondary protection"). Since the lifetime of these materials within this type of corrosive environment is mainly dictated by the secondary regime, the focus of the microstructural investigation is on the propagation following breakaway corrosion.

The results showed that the corrosion attack is indeed very rapid, and that the secondary regime is reached throughout the exposure, i.e., breakaway corrosion occurs rapidly. There is a large difference in the corrosion propagation between the alloys (see Fig. 1c, 4(b, c and d), 5b and 7b), both in extent and in character. However, the corrosion attack may be defined by "general corrosion attack" and/or "steel grain boundary attack". The discussion is therefore divided into two sub-sections, namely "4.1. General corrosion – Oxide scales" and "4.2. Steel grain boundary attack".

4.1. General corrosion – Oxide scales

In a mild environment (e.g., the corresponding dry environment in the absence of KCl(s)) all these materials perform well, forming a protective chromium-rich oxide in the submicron range[9,10,35,36]. This oxide may be referred to as the primary protection of the steel as it is slow-growing, adherent and protects the underlying steel from accelerated corrosion in this environment. However, in more aggressive environments, e.g., in the presence of KCl + H_2O or O_2 + H_2O, this thin protective oxide is deteriorated according to reactions (1) and (2), and breakaway corrosion occurs with high corrosion rates [6,7,9–11,15].

$$Cr_2O_3(s) + 4KCl(s) + 2H_2O(g) + 1.5O_2(g) \rightarrow 2K_2CrO_4(s) + 4HCl(g) \quad (1)$$

$$Cr_2O_3(s) + 2H_2O(g) + 1.5O_2(g) \rightarrow 2CrO_2(OH)_2(g) \quad (2)$$

The oxide thicknesses of the exposed materials in this study indicates that all materials have reached breakaway corrosion within 24 h under these experimental conditions. For 304L, it has been shown that breakaway corrosion occurs already within 1 h in this experimental setup [20]. The chromium-rich oxide initially formed for all these alloys reacted with the KCl-rich environment forming K_2CrO_4 (potassium chromate) and fast-growing oxide scales. The resulting oxide scale is referred to as the secondary protection of the alloy, i.e., this oxide scale serves as the protection against further corrosion attack. The general corrosion is defined as the homogeneous thick scale governed by ion diffusion, i.e., outward-growing iron oxide and inward-growing (Fe, Cr, Ni…) spinel oxide predicted by different diffusivities [15,37].

Overall, the material T91/P91 exhibits the thickest oxide scales among the investigated materials. The materials can be ranked based on the total thickness of oxide formed (including outward- and inward-growing oxides but not the grain boundary attack) as following: T91/P91 > 304L > Sanicro 28 > Inconel 625.

In a recent study, Ni and Cr contents and alloy microstructure were suggested to improve the corrosion properties of the secondary protection, i.e., decrease the growth of the secondary (or breakaway) oxide scale [32]. With low amount of corrosion resistant alloying elements, such as Cr and Ni, the general corrosion of T91/P91 is defined by a thick outward-growing oxide made of hematite and magnetite, and an iron- and chromium-rich inward-growing oxide with an internal oxidation zone at the corrosion front. 304L and Sanicro 28 have, in comparison to

Table 2

Summary of measured oxide scale thickness, oxide scale composition, internal oxidation zone thickness (IOZ) and depth of alloy grain boundary attack (Alloy GB attack).

Material	General corrosion attack				Internal oxidation zone (μm)	Alloy GB attack (μm)
	Outward-growing oxide		Inward-growing oxide			
	Thickness (μm)	Composition	Thickness (μm)	Composition		
P91/T91	15–25	Fe oxides	10–15	Fe-Cr oxide	2.5–3	–
304L	3–5	Fe_2O_3	2–4	Fe-Cr-Ni oxide	–	8–50
Sanicro 28	1–5	Fe-Cr oxide	1–5	Fe-Cr-Ni oxide	–	9–18
Inconel 625	0.5–4	Ni oxide Cr oxide	–	–	1–3	1–11

T91/P91, elevated levels of nickel and chromium, at the expense of iron. This alloying increase of Cr and Ni results in a drastic reduction of the secondary oxide scale thickness for both materials compared to T91/P91. As all of these three materials suffers from breakaway corrosion (i. e., the primary oxide protection is lost) at 600 °C in the presence of KCl almost immediately, it is argued that the differences in oxide thickness after 24 h primarily is an effect of different growth rates of the secondary oxide scale [10,38–40]. However, this decrease is much more prominent when comparing T91/P91 and 304L (from 23 μm to 9 μm total thickness) than 304L and Sanicro 28 (from 9 μm to 6 μm total thickness) which is a smaller decrease of the secondary protection thickness (~33 % decrease compared to ~ 60 % for T91/P91 and 304L). Thus, by adding more Cr and Ni increases the corrosion protection of the secondary scale. However, the greatest decrease is achieved when comparing the ferritic/martensitic T91/P91 to the austenitic alloys 304L and Sanicro 28, implying that the microstructure of the alloy substrate is important. The general corrosion attack of the nickel-based alloy Inconel 625 differs compared to the iron-based steels with respect to the oxide scales formed. The lack (or low levels) of iron in Inconel 625 leads to an outward grown oxide composed of NiO and Cr-oxide, accompanied with K_2CrO_4-particles, compared to the Fe-based steels where the outward growing oxide is composed of Fe-oxides. For Inconel 625, there are also indications of Mo in the outward growing scale. The corrosion attack of this chromia forming alloy is suggested to occur according to (1), which leads to NiO formation after the protective Cr_2O_3 initially formed is destroyed. The inward growing oxide, which for the Fe-based steels are rather homogenous, is for Inconel 625 composed of partly oxidized regions, i.e., an internal oxidation zone composed of Cr-rich oxide and Ni-rich metal. This type of internal oxidation zone morphology is usually seen at the corrosion front [41] or in environments with low partial pressures of oxygen [42]. This is expected as the oxidation of nickel requires rather high oxygen partial pressures [41], compared to Cr and Fe. In Fig. 9, a TEM line scan was performed through this internal oxidation zone. The results show that the internal oxidation zone is composed of Cr-rich oxide and unoxidized metal, which is slightly Cr-depleted and enriched in Mo. In addition, Cl is detected occasionally within this corrosion morphology.

This study highlights that increasing the amount of corrosion resistant alloying elements does not preserve the protectiveness of the primary protection in a KCl-rich environment but decreases the total thickness of the secondary protection. All four investigated materials suffered from breakaway corrosion where the initial protective oxide scale was destroyed, and duplex corrosion scales formed. Thus, from a boiler perspective utilizing KCl-rich fuels this information is important as the lifetime of a material will be dictated by the protectiveness of the secondary oxide scale (i.e., the oxide scale formed after breakaway corrosion) rather than its ability to sustain its primary protection. There was however a trend in less general corrosion, by means of oxide thickness, when increasing the Ni-content at the expense of Fe.

4.2. Steel grain boundary attacks

The second feature that may deteriorate the material is the steel grain boundary attack. The extent of steel grain boundary attack differed substantially between the four investigated materials. For the ferritic/martensitic T91/P91, there is no or very little steel grain boundary attack. Instead, the corrosion front is rather even. This could be a result of the very fast growth of the secondary scale (~15 μm inward-growing scale after 24 h), minimizing the effect of fast diffusion paths as the steel grain boundaries exhibits at these temperatures. Furthermore, as breakaway corrosion is expected to occur swiftly for T91/P91, the fast growth of the secondary scale suggests that there will be little release of chlorine through reaction (1) as the top oxide is very Cr-poor. It was recently shown that Cl plays an important role in the steel grain boundary attack of 304L in this environment [20]. The lack of steel grain boundary attack on T91/P91 may also be a result of the structure of this

steel, being ferritic/martensitic (compared to the other materials which all are austenitic). For the austenitic stainless steels and nickel-based alloy (304L, Sanicro 28 and Inconel 625), the increasing Cr/Fe ratio would sustain the reaction (1) leading to a higher chlorine load and therefore a steel grain boundary attack being much more pronounced, in relation to the general corrosion attack.

The observed steel grain boundary attack on the four investigated materials showed that an increase in corrosion resistant alloying elements does not lead to an avoidance of grain boundary attacks. Contrary to the general corrosion, the steel grain boundary attack remains strongly present for all the austenitic materials, regardless of alloying content. However, the morphology or type of grain boundary attacks were rather different. For 304L and Sanicro 28, the grain boundary attack changed its corrosion morphology. For both materials, the attack was defined by a narrow internal oxidation and the presence of nickel-rich nodules at the grain boundaries. In addition, some small voids were observed in the grain boundary attack, slightly more accentuated for Sanicro 28 compared to 304L. There were also indications of the grain boundary attack of 304L being the initiation point for oxidization of the bulk grain, i.e., the grain boundary attack is no longer defined by a narrow oxidation zone but instead the grows laterally. As this was mostly observed at the part of the grain boundary attack closer to the surface, the grain boundary attack seems to be diffusion controlled. In contrast to the three other materials, the steel grain boundary attack of Inconel 625 is primarily defined by void formation at the grain boundaries instead of internal oxidation. It is argued that difference between the 304L, Sanicro 28 and Inconel 625 with respect towards GB attack is due primarily to the amount of Fe (or lack of Ni) in the material. With an increasing amount of Ni, on the expense of Fe, the number of voids at the GBs increased. This is suggested to be coupled to the low oxidation potential of Ni. For 304L, with a high Fe/Ni ratio, the GB is being oxidized by Fe-oxides.

Regardless of material, chlorine was detected in connection to the grain boundary attack. For 304L and Sanicro 28 only cross-sectional SEM/EDX were performed and only indications of chlorine in the GB attack was seen. For Inconel 625, detailed TEM analysis was in addition performed. The TEM analysis revealed that chlorine was detected within the internal oxidation zone oxide as well as in the alloy grain boundaries. In fact, chlorine was especially enriched in the alloy grain boundaries. The presence of Cl in the GB's is suggested to accelerate the GB attack. In a recent study of 304L in this type of KCl-rich environment the alloy grain boundary attack was followed closely using 3D-FIB and TEM [20]. As in the current study, only small amounts of chlorine were detected for 304L at the alloy grain boundaries. The study showed that the alloy microstructure close to the GB's was depleted (in primarily Cr) and that in the presence of chlorine, rapid diffusion was observed. In the present study, the TEM analysis of Inconel 625 did indeed detect Cl in the grain boundaries. But also, Cl was sporadically detected throughout the internal oxidation zone.

In chlorine containing exposures, the active oxidation mechanism is often referred to in order for explaining the corrosion acceleration [5]. This mechanism suggests that the corrosion is driven by the formation of chlorine gas (Cl_2 (g)) at the scale gas interface which is diffusing through the oxide scale towards the metal/oxide interface. At this interface, chlorine gas reacts with metal to form its corresponding metal chloride, which at high temperatures is volatile, and will diffuse outwards through the oxide scale as $MeCl_x$ (g) (e.g., $FeCl_2$ (g)). As this gaseous molecule is transported outwards through the oxide scale it will react with oxygen as the oxygen partial pressure is increased through the scale. As the gaseous metal chloride reacts with oxygen, corresponding metal oxide forms as well as Cl_2 (g). This newly formed Cl_2 (g) can diffuse towards the metal/oxide interface, in a cyclic behavior. According to this mechanism, the corrosion acceleration caused by chlorine is due to this cyclic behavior of gases, compared to the oxidation which is based on ion diffusion through the oxide scale. However, in order for this mechanism to work, the gaseous diffusion of Cl_2 and $MeCl_x$

through the oxide scale must be much faster than O_2 (g). Otherwise, the necessary oxygen gradient over the oxide scale, needed to form metal chlorides rather than metal oxides, is impossible to maintain. Furthermore, since the transport is suggested to occur by gaseous species, cracks, connected voids or microcracks is needed. However, based on the sizes of O_2 (covalent radius: 66 pm) and Cl_2 (covalent radius: 102 pm) it is unlikely that the smaller oxygen gas molecule is disallowed to enter through the scale whereas the larger chlorine gas molecule is not. In fact, A.G. Guy showed the opposite when studying gas osmosis, a smaller gas molecule can pass through a small-pores membrane whereas the larger gas molecule cannot [43].

Based on the observed results in the present study, it is clear that chlorine has accelerated the corrosion attack of both the grain boundaries and the general corrosion attack. According to the TEM analysis of Inconel 625, see Figs. 8 and 9, Cl was detected both in the alloy grain boundaries but also in the internal oxidation zone. It is suggested that the chlorine is diffusing inwardly as a chlorine ion, Cl^-, driven by the normal oxidation potential that the material experience [29]. In the article referred to, DFT calculations were deployed in order elucidate different steps/reactions of the inward diffusion of chlorine. The net reaction is however summed up as:
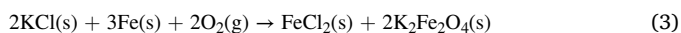
$$2KCl(s) + 3Fe(s) + 2O_2(g) \rightarrow FeCl_2(s) + 2K_2Fe_2O_4(s) \tag{3}$$

The acceleration of the corrosion attack caused by chlorine is suggested to occur by chlorine increasing the diffusion properties of the scale, as the corrosion in the presence of chlorine still shows characteristics of a diffusion-controlled attack. However, the exact distribution and role of chlorine in the grain boundary attack as well as in the general corrosion needs to be studied further.

Summarizing the alloy GB attack of the four alloys investigated within this study, it is clear that the alloy composition and microstructure have an impact on the outcome and extent of this type of corrosion attack. For the ferritic-martensitic P91/T91, there were no alloy GB attack whereas all three austenitic alloys (304L, Sanicro 28 and Inconel 625) suffered from severe alloy GB attack. The alloy GB attack was often associated with the presence of Cl, even though it was not always detected in the attack. With a more detailed microscopy analysis (TEM), the presence of Cl in the GB's was clearly detected, up to 10 %.

5. Summary

The aim of this study was to investigate the corrosion behavior of four commercial alloys in a harsh KCl-rich environment: T91/P91, 304L, Sanicro 28 and Inconel 625. The materials were exposed in an experimental setup utilizing a continuous deposition of KCl(s) on the sample surface. This type of corrosive environment becomes more and more important to study and understand as the fuel feedstock becomes more influenced by agricultural and forest residues as well as waste fuels rather than clean biomass. This experimental setup aims to mimic the harsh conditions experienced by the superheaters in boilers using KCl-rich fuels. The reproducibility of this experimental setup and comparison to other KCl-containing laboratory exposures as well as a 12 MW waste fired boiler was recently published in [21].

The results were discussed in two sections focusing on the specific type of corrosion attack: general corrosion (growth of secondary protection covering the sample surface) and steel grain boundary attack for four commercial high temperature alloys.

Considering the general corrosion, a drastic decrease of the secondary protection thickness was observed when increasing the amount of corrosion resistant alloying elements, from 30 μm for T91/P91, 5–7 μm for 304L and Sanicro 28 to about 3 μm for Inconel 625. Despite different oxide thicknesses all four materials have lost their primary protection, i. e., a chromium-rich corundum type oxide in the submicron range. Instead, the materials have entered the secondary regime with the formation of thick duplex oxide layers. These oxide scales for the different materials were composed of:

T91/P91 formed a thick layer of outward growing magnetite (Fe_3O_4) and hematite (Fe_2O_3) as well as a thick inward-growing spinel oxide (Fe, Cr)$_3O_4$. The total thickness was about 30 μm.

The stainless steels, 304L and Sanicro 28, experienced a similar attack and the oxide scales consisted of an outward growing hematite layer. For Sanicro 28, this layer was doped with some chromium. For both steels, the inward-growing oxide consisted of a ((Cr,Fe,Ni)$_3O_4$) spinel oxide. The total thickness was about 7 and 5 μm for 304L and Sanicro 28, respectively.

The nickel-based alloy Inconel 625 exhibited slightly different oxide scales compared to other materials. The outward growing oxide scale was composed of NiO together with Cr_2O_3. The inward growing scale was composed of fully oxidized, instead the scale was composed of selectively oxidized Cr_2O_3 whereas Ni remained unoxidized, a so-called internal oxidation zone. The total thickness was about 3 μm.

For all four materials, the results suggest that the general corrosion attack by KCl was initiated by the formation of chromate, K_2CrO_4, and thereby destroying the chromium rich oxide, i.e., the primary protection scale. This leads to fast oxidation rates and thick oxide scales, i.e., the secondary corrosion regime. There were however rather large discrepancies in corrosion rate/oxide thickness where the ferritic T91/P91 (having the highest Fe/Cr ratio in the alloy) performed worst and the austenitic nickel-based alloy Inconel 625 (with the lowest Fe/Cr ratio) performed best.

Summarizing the alloy GB attack of the four alloys investigated within this study, it is clear that the alloy composition and microstructure have an impact on the outcome and extent of this type of corrosion attack. For the ferritic-martensitic P91/T91, there were no alloy GB attack whereas all three austenitic alloys (304L, Sanicro 28 and Inconel 625) suffered from severe alloy GB attack. The alloy GB attack was often associated with the presence of Cl, even though it was not always detected in the attack. The alloy GB attack for the austenitic alloys can be summarized as follows:

The alloy GB attack of 304L were 11–50 μm in depth and characterized by being fully oxidized, even though some porosity existed.

For Sanicro 28, the GB attack was not as deep, about 9–18 μm. Also, the attack included a higher degree of voids compared to 304L.

Inconel 625 exhibited grain boundary attacks characterized primarily by void formation and the development of large cavities. The depth of the GB attack was 1–11 μm.

Based on the observed results in the present study, it is clear that chlorine has accelerated the corrosion attack of both the grain boundaries and the general corrosion attack. The acceleration of the corrosion attack caused by chlorine is suggested to occur by chlorine increasing the diffusion properties of the scale, as the corrosion in the presence of chlorine still shows characteristics of a diffusion-controlled attack.

CRediT authorship contribution statement

J. Phother-Simon: . **I. Hanif:** Investigation. **T. Jonsson:** Writing – review & editing, Writing – original draft, Supervision, Conceptualization. **J. Liske:** Writing – review & editing, Writing – original draft, Supervision, Project administration, Funding acquisition, Conceptualization.

Declaration of Competing Interest

The authors declare the following financial interests/personal relationships which may be considered as potential competing interests: [Jesper Liske reports financial support was provided by Swedish Energy Agency].

Data availability

Data will be made available on request.

References

[1] Arnell NW, Brown S, Gosling SN, Gottschalk P, Hinkel J, Huntingford C, et al. The impacts of climate change across the globe: A multi-sectoral assessment. Clim Change 2016;134(3):457–74.

[2] Kassman H, Pettersson J, Steenari B-M, Åmand L-E. Two strategies to reduce gaseous KCl and chlorine in deposits during biomass combustion—Injection of ammonium sulphate and co-combustion with peat. Fuel Process Technol 2013;105: 170–80.

[3] Nielsen HP, Frandsen FJ, Dam-Johansen K, Baxter LL. The implications of chlorine-associated corrosion on the operation of biomass-fired boilers. Prog Energy Combust Sci 2000;26(3):283–98.

[4] Enestam S, Bankiewicz D, Tuiremo J, Mäkelä K, Hupa M. Are NaCl and KCl equally corrosive on superheater materials of steam boilers? Fuel 2013;104:294–306.

[5] Grabke HJ, Reese E, Spiegel M. The effects of chlorides, hydrogen chloride, and sulfur dioxide in the oxidation of steels below deposits. Corros Sci 1995;37(7): 1023–43.

[6] Pettersson J, Folkeson N, Johansson L-G, Svensson J-E. The effects of KCl, K2SO4 and K2CO3 on the high temperature corrosion of a 304-type austenitic stainless steel. Oxid Met 2011;76(1):93–109.

[7] Sui J, Lehmusto J, Bergelin M, Hupa M. The effects of KCl, NaCl and K2CO3 on the high-temperature oxidation onset of sanicro 28 steel. Oxid Met 2016;85(5):565–98.

[8] Okoro SC, Montgomery M, Frandsen FJ, Pantleon K. High temperature corrosion during biomass firing: improved understanding by depth resolved characterisation of corrosion products. Mater High Temp 2015;32(1–2):92–101.

[9] Lehmusto J, Yrjas P, Skrifvars BJ, Hupa M. High temperature corrosion of superheater steels by KCl and K2CO3 under dry and wet conditions. Fuel Process Technol 2012;104:253–64.

[10] Pettersson J, Asteman H, Svensson J-E, Johansson L-G. KCl induced corrosion of a 304-type austenitic stainless steel at 600°C; The role of potassium. Oxid Met 2005; 64(1):23–41.

[11] Kiamehr S, Dahl KV, Montgomery M, Somers MAJ. KCl-induced high temperature corrosion of selected commercial alloys. Mater Corros 2015;66(12):1414–29.

[12] Davidsson KO, Åmand L-E, Leckner Bo, Kovacevik B, Svane M, Hagström M, et al. Potassium, chlorine, and sulfur in ash, particles, deposits, and corrosion during wood combustion in a circulating fluidized-bed boiler. Energy Fuel 2007;21(1): 71–81.

[13] Karlsson S, Åmand L-E, Liske J. Reducing high-temperature corrosion on high-alloyed stainless steel superheaters by co-combustion of municipal sewage sludge in a fluidised bed boiler. Fuel 2015;139:482–93.

[14] N. Folkeson J. Pettersson C. Pettersson L.G. Johansson et al. Fireside corrosion of stainless and low alloyed steels in a waste-fired CFB boiler The effect of adding sulphur to the fuel. in Materials Science Forum. 2008. Trans Tech Publ.

[15] Jonsson T, Karlsson S, Hooshyar H, Sattari M, Liske J, Svensson J-E, et al. Oxidation after breakdown of the chromium-rich scale on stainless steels at high temperature: Internal oxidation. Oxidation of Metals 2016;85(5-6):509–36.

[16] Antunes RA, de Oliveira MCL. Corrosion in biomass combustion: A materials selection analysis and its interaction with corrosion mechanisms and mitigation strategies. Corros Sci 2013;76:6–26.

[17] Michelsen HP, Frandsen F, Dam-Johansen K, Larsen OH. Deposition and high temperature corrosion in a 10 MW straw fired boiler. Fuel Process Technol 1998;54 (1):95–108.

[18] Montgomery M, Karlsson A. In-situ corrosion investigation at Masnedø CHP plant–A straw-fired power plant. Mater Corros 1999;50(10):579–84.

[19] Persdotter A, Sattari M, Larsson E, Olivas Ogaz MA, Liske J, Jonsson T. Oxidation of Fe-2.25Cr-1Mo in presence of KCl(s) at 400 °C – Crack formation and its influence on oxidation kinetics. Corros Sci 2020;163:108234.

[20] Phother-Simon J, Hanif I, Liske J, Jonsson T. The influence of a KCl-rich environment on the corrosion attack of 304 L: 3D FIB/SEM and TEM investigations. Corros Sci 2021;183:109315.

[21] Phother-Simon J, Jonsson T, Liske J. Continuous KCl addition in high temperature exposures of 304 L – A way to mimic a boiler environment. Corros Sci 2020;167: 108511.

[22] Abels JM, Strehblow HH. A surface analytical approach to the high temperature chlorination behaviour of inconel 600 at 700 °C. Corros Sci 1997;39(1):115–32.

[23] McNallan M, Liang W, Kim S, Kang C. Acceleration of the high temperature oxidation of metals by chlorine. in International Corrosion Conference Series 1983: NACE.

[24] Shinata Y. Accelerated oxidation rate of chromium induced by sodium chloride. Oxid Met 1987;27(5):315–32.

[25] Wang C-J, He T-T. Morphological development of subscale formation in Fe–Cr–(Ni) alloys with chloride and sulfates coating. Oxid Met 2002;58(3):415–37.

[26] Zahs A, Spiegel M, Grabke HJ. Chloridation and oxidation of iron, chromium, nickel and their alloys in chloridizing and oxidizing atmospheres at 400–700°C. Corros Sci 2000;42(6):1093–122.

[27] Sanusi T, Sumner J, Simms NJ. A comparative evaluation of waste wood and herbaceous biomass fireside corrosion behaviours. Fuel 2022;324:124070.

[28] Folkeson N, Johansson L-G, Svensson J-E. Initial stages of the HCl-induced high-temperature corrosion of alloy 310. J Electrochem Soc 2007;154(9):C515.

[29] Cantatore V, Olivas Ogaz MA, Liske J, Jonsson T, Svensson J-E, Johansson L-G, et al. Oxidation driven permeation of iron oxide scales by chloride from experiment guided first-principles modeling. J Phys Chem C 2019;123(42):25957–66.

[30] Jonsson T, Folkeson N, Svensson JE, Johansson LG, Halvarsson M. An ESEM in situ investigation of initial stages of the KCl induced high temperature corrosion of a Fe–2.25Cr–1Mo steel at 400°C. Corros Sci 2011;53(6):2233–46.

[31] Niemi J, Engblom M, Laurén T, Yrjas P, Lehmusto J, Hupa M, et al. Superheater deposits and corrosion in temperature gradient – Laboratory studies into effects of flue gas composition, initial deposit structure, and exposure time. Energy 2021; 228:120494.

[32] Persdotter A, Eklund J, Liske J, Jonsson T. Beyond breakaway corrosion – Influence of chromium, nickel and aluminum on corrosion of iron-based alloys at 600 °C. Corros Sci 2020;177:108961.

[33] Folkeson N, Pettersson J, Pettersson C, Johansson LG, Skog E, Andersson BÅ, et al. Fireside corrosion of stainless and low alloyed steels in a waste-fired CFB boiler; The effect of adding sulphur to the fuel. Mater Sci Forum 2008;595-598:289–97.

[34] Andersson S, Blomqvist EW, Bäfver L, Jones F, Davidsson K, Froitzheim J, et al. Sulfur recirculation for increased electricity production in waste-to-energy plants. Waste Manag 2014;34(1):67–78.

[35] Ehlers J, Young DJ, Smaardijk EJ, Tyagi AK, Penkalla HJ, Singheiser L, et al. Enhanced oxidation of the 9%Cr steel P91 in water vapour containing environments. Corros Sci 2006;48(11):3428–54.

[36] Pettersson C, Jonsson T, Proff C, Halvarsson M, Svensson J-E, Johansson L-G. High temperature oxidation of the austenitic (35Fe27Cr31Ni) alloy sanicro 28 in O 2+ H 2 O environment. Oxid Met 2010;74(1–2):93–111.

[37] Jonsson T, Larsson H, Karlsson S, Hooshyar H, Sattari M, Liske J, et al. High-temperature oxidation of FeCr (Ni) alloys: The behaviour after breakaway. Oxid Met 2017;87(3-4):333–41.

[38] Liu B, Chen X. Impacts of temperature and KCl on corrosion behavior of 12Cr1MoVG and T91 in HCl-containing atmosphere. Oxid Met 2018;90(5):585–97.

[39] Pettersson C, Johansson LG, Svensson JE. The influence of small amounts of KCl(s) on the initial stages of the corrosion of alloy sanicro 28 at 600 °C. Oxid Met 2008; 70(5):241–56.

[40] Karlsson S, Jonsson T, Hall J, Svensson J-E, Liske J. Mitigation of fireside corrosion of stainless steel in power plants: A laboratory study of the influences of SO2 and KCl on initial stages of corrosion. Energy Fuel 2014;28(5):3102–9.

[41] Jonsson T, Larsson H, Karlsson S, Hooshyar H, Sattari M, Liske J, et al. High-temperature oxidation of FeCr(Ni) Alloys: The behaviour after breakaway. Oxid Met 2017;87(3-4):333–41.

[42] Hooshyar H, Jonsson T, Hall J, Svensson JE, Johansson LG, Liske J. The effect of H2 and H2O on the oxidation of 304L-stainless steel at 600 °C: General behaviour (Part I). Oxid Met 2016;85(3):321–42.

[43] Guy AG. Osmosis in gases. Appl Phys Commun 1989;9(1–2):115–27.